DEVELOPMENT AND WAVELENGTH CALIBRATION OF A VIS–NIR PUSHBROOM HYPERSPECTRAL IMAGING SYSTEM WITH EXPERIMENTAL ANALYSIS OF SMILE AND KEYSTONE DISTORTIONS

Ahmed Fawzy Hussein[1] *Ali AlBeladi*[1,2]

[1]Department of Electrical Engineering, KFUPM, 31261, Saudi Arabia
[2]Center for Intelligent Manufacturing & Robotics, KFUPM, Dhahran 31261, Saudi Arabia

ABSTRACT

This paper presents an upgraded VIS–NIR pushbroom hyperspectral imaging (HSI) system covering 400–1000 nm and its experimental calibration. The system uses C-mount optics, a 300 grooves/mm transmission grating, and a custom 3D-printed cage. Wavelength calibration with a halogen source and narrow-band filters was performed at the center, left, and right positions of the slit. The wavelength-to-pixel mapping varied across the field, with a maximum wavelength error of 38 nm and left/right spatial RMSE values of 49.08/53.06 pixels relative to the center ($R^2 = 0.9909/0.9894$). These results demonstrate that a single global wavelength calibration is insufficient for accurate hyperspectral cube reconstruction and that spatially dependent geometric correction is required. The proposed system and calibration framework provide a practical foundation for subsequent smile and keystone correction and for reliable quantitative VIS–NIR hyperspectral imaging applications.

Index Terms— VIS–NIR Pushbroom hyperspectral imaging, wavelength calibration, smile distortion, keystone distortion, geometric analysis.

1. INTRODUCTION

Hyperspectral imaging (HSI) records a spectrum at each spatial location, enabling material characterization from wavelength-dependent responses. Pushbroom systems acquire these data sequentially and can be built from commercially available components, offering a flexible, lower-cost alternative to dedicated instruments [1–4]. Their measurement accuracy, however, depends on optical alignment and calibration.

Two important geometric distortions are smile, which causes wavelength positions to vary across the spatial dimension, and keystone, which shifts corresponding spatial features between spectral bands. Both can impair spectral assignment and spatial registration [5–8]. A calibration measured at only one spatial position may not capture these variations across the detector; optical alignment and other geometric effects can also contribute to spatially varying errors [9, 10].

This work presents an upgraded VIS–NIR pushbroom HSI system operating over 400–1000 nm, building on our earlier low-cost system and related acquisition work [11, 12]. The instrument uses higher-performance C-mount objectives, a 300 grooves/mm blazed transmission grating, and a custom 3D-printed optical–mechanical cage. To characterize spatial variation, we calibrate at the center, left, and right detector positions using a halogen source and narrow-band filters. These measurements support the analysis and correction of spatially dependent wavelength errors.

The main contributions are:

- Design and implementation of an upgraded VIS–NIR pushbroom HSI system using commercially available components and a custom 3D-printed assembly.
- Multi-position calibration and quantitative characterization of spatially dependent wavelength errors associated with smile and keystone distortions.

2. HSI HIGH-QUALITY SYSTEM DEVELOPMENT (VERSION 2)

The proposed HSI system was constructed using commercially available components and a custom 3D-printed housing to achieve a balance between performance, modularity, and cost. The optical assembly consists of an area-scan camera, an entrance slit, three VIS-NIR C-mount objectives, and a reflective diffraction grating arranged in a Czerny–Turner configuration [13]. The detector was selected for its high sensitivity across the 400-1000 nm spectral range. The full list is provided in Table 1.

The optical path follows a standard pushbroom architecture in which the scene is focused onto the entrance slit, collimated, spectrally dispersed by the diffraction grating, and reimaged onto the detector. Spatial information is recorded along one detector axis, while wavelength information is encoded along the orthogonal axis. A custom 3D-printed enclo-

Corresponding author: Ahmed Fawzy Hussein (e-mail: g202391210@kfupm.edu.sa).

sure provides precise optical alignment, mechanical stability, and reduced stray-light interference.

Figure 1 shows the design of the complete HSI_{V2} system, using SolidWorks software.

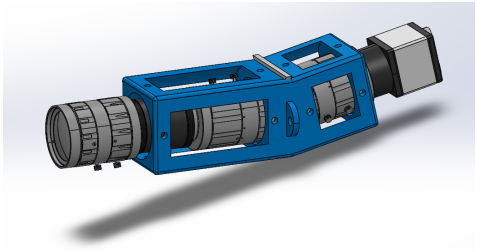


Fig. 1: HSI_{V2} Design using SolidWorks

2.1. System Overview

The pushbroom HSI module comprises high-quality VIS–NIR C-mount objectives, a 300 lines/mm blazed diffraction grating arranged in a Czerny–Turner configuration, an area-scan camera, and a custom 3D-printed cage for precise optical alignment and mechanical stability. The optical path focuses the scene onto an entrance slit, collimates the light, disperses it using the diffraction grating, and reimages the spectrum onto the detector. The detector records spatial information along one axis and spectral information along the orthogonal axis. The complete hardware configuration is provided in Table 1.

2.2. Mechanical Assembly

The optical components are mounted within a custom 3D-printed PLA chassis designed to provide mechanical stability, precise optical positioning, and reduced internal reflections and stray light. The cage-based design integrates the slit, collimating optics, diffraction grating, and detector into a rigid and modular optical assembly.

The assembly procedure includes pre-focusing the C-mount objectives to infinity and securing their focus positions, followed by alignment of the diffraction grating, entrance slit, collimating optics, and detector. The HSI_{V2} employs a 300 grooves/mm transmission diffraction grating blazed at $17.5°$, providing efficient VIS–NIR spectral dispersion over the 400–1000 nm range. For the first diffraction order ($k = 1$) and a central wavelength of $\lambda_c = 700$ nm, the expected diffraction angle is calculated as

$$\beta = \arcsin\left(\frac{k\lambda_c}{a}\right) \approx 0.212 \text{ rad} \approx 12.1°, \tag{1}$$

where $a = 3.33$ μm is the grating groove spacing. This calculation provides the initial alignment reference for the spectrograph. The entrance slit and collimating optics are positioned to maintain the required focal geometry, with a nominal back focal distance of 17.526 mm between the lens and slit plane. The distance from the back side of the slit holder to the opposite end of the lens tube should be approximately 11 mm. This arrangement places the slit roughly 12.7 mm from each edge of the lens tube. Fig. 2 shows the slit and slit tube assembly.

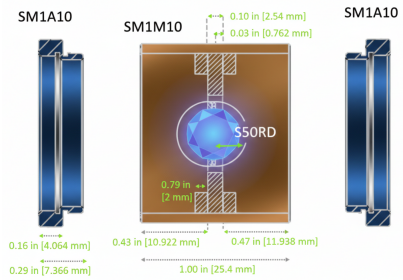


Fig. 2: Slit and Slit Tube Assembly [13]

The resulting configuration provides stable optical alignment while supporting spectral resolution and uniform illumination across the detector plane [13].

2.3. Data Acquisition and Preprocessing

Hyperspectral data were acquired using a stationary line-scan camera and a V-Slot® linear stage under halogen illumination. The halogen source provides broadband illumination across the VIS–NIR spectral range and was used together with calibrated bandpass filters to generate reference spectral peaks for wavelength calibration.

For an HSI cube of dimensions (H, W, B), the spatially averaged spectral response at the i-th spectral band was calculated as

$$S(\lambda_i) = \frac{1}{HW}\sum_{x=1}^{H}\sum_{y=1}^{W} I(x, y, \lambda_i), \tag{2}$$

where $I(x, y, \lambda_i)$ denotes the measured intensity at spatial position (x, y) and spectral band λ_i. The resulting spectral profile was used to identify the locations of the reference spectral peaks.

Wavelength calibration was performed using narrow-band optical filters with nominal wavelengths of 410, 460, 510, 560, 610, 660, 710, 760, 860, 910, 960, and 1000 nm. For each filter, the corresponding spectral peak was identified and its detector pixel position p_i was recorded, forming a set of reference pairs $\{(p_i, \lambda_i)\}$.

The pixel-to-wavelength relationship was initially determined by linear interpolation between adjacent reference points (p_1, λ_1) and (p_2, λ_2):

$$\lambda(p) = \frac{\lambda_2 - \lambda_1}{p_2 - p_1}(p - p_1) + \lambda_1. \tag{3}$$

Item #	Name	Description	Quantity	Cost ($)	Link
1	GS3-U3-41C6NIR-C	FLIR Grasshopper®3 High Performance USB 3.0 NIR Camera, 1”	1	1540	Link
2	EO#67-717	50mm C VIS-NIR Series Fixed Focal Length Lens	2	1190	Link
3	EO#39-939	6mm C VIS-NIR Series Fixed Focal Length Lens	1	595	Link
4	Thorlabs S50RD	S50LK Ø1” Mounted Slit, 50 ± 3 µm Wide, 10 mm Long	1	121.72	Link
5	Thorlabs SM1M10	SM1 lens tube 1” long with internal threads and retaining rings	1	16.96	Link
6	Thorlabs SM1A10	Adapter ring SM1 to C-mount internal	2	44.52	Link
7	EO#49-579	25 mm square, 17.5° blazed transmission grating (300 lines/mm)	1	117	Link
8	Grating holder	3D printed HSI holder	1	-	Link
			Total	3625.2	

Table 1: Hardware components for HSI system setup with quantity, cost, and reference links.



Fig. 3: HSI_{V2} full system configuration.

This calibration establishes the mapping between detector pixel position and physical wavelength and provides the reference spectral coordinate system used for subsequent analysis of spatially dependent wavelength errors and geometric distortions.

3. EXPERIMENTAL RESULTS AND DISCUSSION (REAL HSI DATA)

Figure 3 shows the complete HSI_{V2} system configuration.

Prior to calibration, the lens focus was adjusted using a Macbeth ColorChecker to obtain clearly distinguishable spectral features. A halogen lamp was then used as the broadband illumination source, and narrow-band optical filters were sequentially introduced to generate reference spectral peaks at predefined wavelengths. The corresponding detector pixel positions were extracted from the acquired spectra and associated with the nominal filter wavelengths. Figure 4 shows a representative spectrum acquired using the 760 nm filter.

To characterize spatially dependent spectral distortions,

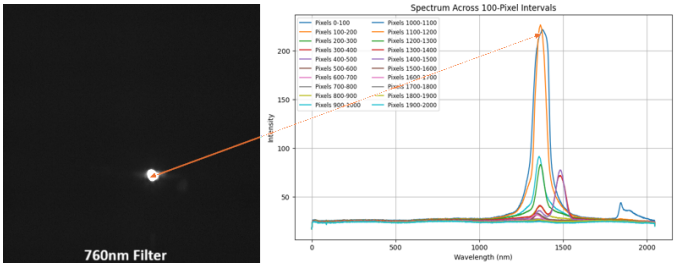


Fig. 4: Experimental spectrum acquired using the 760 nm bandpass filter.

wavelength calibration measurements were performed at three positions across the slit: center (n), left (n_l), and right (n_r). For each reference wavelength, the corresponding detector pixel position was recorded at all three spatial locations. Table 2 summarizes the measured pixel positions and the associated wavelength and spatial errors.

The calibration results show that the pixel position corresponding to a given wavelength varies across the slit. These spatially dependent deviations indicate the presence of geometric distortions, including keystone and smile effects. The magnitude of the deviations also varies with wavelength, demonstrating that the spectral mapping is not spatially uniform across the detector. Therefore, spatially dependent geometric correction is required in addition to wavelength calibration to achieve accurate wavelength assignment and spatial registration in the reconstructed hyperspectral cube.

To quantify these spatial variations, absolute and relative errors were calculated between the center reference position (n) and the corresponding left (n_l) and right (n_r) measurements.

The error analysis confirms systematic spatial variations in the spectral mapping across the detector field of view. Both the left (n_l) and right (n_r) measurements exhibit consistent offsets relative to the center reference (n), demonstrating that a single wavelength-to-pixel relationship cannot accurately represent all spatial positions. As shown in Table 2, the largest relative pixel-position errors occur at shorter wavelengths, exceeding 10% in some cases, whereas the errors generally de-

Table 2: Wavelength calibration and spatial errors between the center, left, and right positions before distortion correction. λ is the reference wavelength, n, n_l, and n_r are the corresponding pixel positions at the center, left, and right positions, respectively. λ_l' and λ_r' are the interpolated wavelengths at the left and right positions, while err_l and err_r represent the absolute wavelength errors. AbsErr_{n_l} and AbsErr_{n_r} represent the absolute pixel-position errors relative to the center.

λ **(nm)**	n	n_l	λ_l' **(nm)**	err_l **(nm)**	n_r	λ_r' **(nm)**	err_r **(nm)**	AbsErr_{n_l}	AbsErr_{n_r}	RelErr_{n_l} **(%)**	RelErr_{n_r} **(%)**
410	392	351	394	16	344	391	19	-41	-48	-10.459	-12.245
460	519	455	435	25	453	434	26	-64	-66	-12.331	-12.717
510	672	635	498	12	626	495	15	-37	-46	-5.506	-6.845
560	812	788	551	9	781	549	11	-24	-31	-2.956	-3.818
610	962	926	598	12	907	592	18	-36	-55	-3.742	-5.717
660	1096	1051	643	17	1035	637	23	-45	-61	-4.106	-5.566
710	1238	1193	694	16	1184	691	19	-45	-54	-3.635	-4.362
760	1373	1321	741	19	1335	746	14	-52	-38	-3.787	-2.768
800	1461	1394	770	30	1377	762	38	-67	-84	-4.586	-5.749
860	1640	1606	849	11	1604	848	12	-34	-36	-2.073	-2.195
910	1795	1739	892	18	1744	894	16	-56	-51	-3.120	-2.841
960	1918	1864	938	22	1870	940	20	-54	-48	-2.815	-2.503
1000	2030	1968	978	22	1980	982	18	-62	-50	-3.054	-2.463

crease to approximately 2–5% at longer wavelengths. This wavelength-dependent behavior indicates that the geometric distortion is more pronounced toward the lower end of the spectral range.

The unequal deviations between the left and right positions further indicate that the distortion is asymmetric and cannot be described solely by a uniform linear displacement. The observed spatial and wavelength-dependent variations are consistent with the combined effects of keystone and smile distortions. These results demonstrate that spatially uniform wavelength calibration is insufficient for the current system and that geometric correction is required to improve wavelength assignment and spatial registration in the reconstructed hyperspectral cube.

To further quantify calibration consistency, statistical error metrics were calculated by comparing the left (n_l) and right (n_r) measurements with the center reference (n). The results are summarized in Table 3. The negative residual means for both spatial positions indicate that the detected pixel locations are systematically shifted toward lower pixel values relative to the center reference, confirming the presence of a spatial bias in the spectral mapping.

Metric	n_l **vs** n **(Left)**	n_r **vs** n **(Right)**
Residual Mean	-47.4615	-51.3846
Residual Std	13.0039	13.7692
RMSE	49.0784	53.0602
Relative RMSE	0.0401	0.0434
R^2	0.9909	0.9894

Table 3: Statistical error metrics for wavelength calibration at left and right spatial positions relative to the center reference.

The statistical analysis further confirms the presence of systematic spatial distortion in the hyperspectral imaging system. The RMSE values are 49.08 pixels for the left position and 53.06 pixels for the right position relative to the center reference, with the slightly larger error on the right indicating asymmetric spatial distortion. Although the relative RMSE is approximately 4%, the magnitude of the spatial displacement can affect wavelength assignment and spatial registration within the reconstructed hyperspectral cube.

In contrast, the coefficients of determination remain high for both positions ($R^2 = 0.9909$ for the left and $R^2 = 0.9894$ for the right), indicating that the wavelength-to-pixel relationship remains predominantly linear despite the systematic spatial offsets. This combination of strong linearity and spatially dependent displacement is consistent with keystone distortion, while the residual variations between spatial positions suggest additional curvature associated with smile distortion.

Overall, the results demonstrate that the system maintains strong spectral linearity but exhibits significant spatially dependent calibration errors. These findings establish the need for spatially dependent smile and keystone correction to improve wavelength assignment, spatial registration, and the reliability of quantitative hyperspectral measurements.

We evaluated the correction using [describe the validation measurement and identify which reference wavelengths were held out]. Before correction, the maximum wavelength-assignment error was 38 nm. After correction, it was 8 nm. The left and right spatial RMSE values decreased from 49.08 and 53.06 pixels to 11.37 and 9.89 pixels, respectively; the corrected mapping had $R^2 > 0.999$. The complete calibration and correction workflow is reported in [14].

4. CONCLUSION

This work presented an upgraded VIS–NIR pushbroom hyperspectral imaging system covering 400–1000 nm and characterized its wavelength mapping at three spatial positions. Building on the low-cost $\mathrm{HSI}_{\mathrm{V1}}$ system, $\mathrm{HSI}_{\mathrm{V2}}$ incorpo-

rates an upgraded optical configuration, including higher-performance C-mount objectives, a 300 grooves/mm blazed transmission grating, and a newly designed 3D-printed cage. An experimental wavelength calibration procedure was established using a halogen illumination source and narrow-band optical filters distributed across the operating spectral range. The calibration measurements demonstrated a predominantly linear spectral response; however, significant spatial variations in the wavelength-to-pixel mapping were observed at the center, left, and right positions of the slit. The maximum observed wavelength deviation reached 38 nm, while the spatial calibration errors resulted in RMSE values of 53.06 pixels and 49.08 pixels for the right and left positions, respectively, relative to the center reference, with R^2 values ranging from 0.989 to 0.991. Overall, the proposed system and experimental calibration framework provide a practical foundation for accurate VIS–NIR hyperspectral imaging. The characterization of spatially varying spectral errors establishes the basis for subsequent smile and keystone correction, with the objective of improving wavelength assignment, spatial registration, and the reliability of quantitative spectral analysis. The developed HSI platform combines modularity, improved optical and mechanical design, and relatively low cost, making it suitable as a foundation for future hyperspectral imaging applications.

5. ACKNOWLEDGMENTS

This work was supported by King Fahd University of Petroleum and Minerals (KFUPM) through the University Funded Grant no. EC231006.

6. REFERENCES

[1] A.-K. Mahlein, "Plant disease detection by hyperspectral imaging: Focus on signal quality for classification accuracy," *Plant Methods*, vol. 12, p. 35, 2016.

[2] A. F. Hussein, W. M. Hamanah, and M. A. Abido, "Harnessing hyperspectral imaging and deep learning for advanced e-waste classification using three spectral bands," *Results in Engineering*, vol. 27, p. 106110, 2025.

[3] M. B. Henriksen, F. Sigernes, and T. A. Johansen, "A closer look at a spectrographic wavelength calibration." in *WHISPERS*, 2022, pp. 1–5.

[4] A. Al-Hourani, S. Balendhran, S. Walia, and T. Hourani, "Line Scan Hyperspectral Imaging Framework for Open Source Low-Cost Platforms," *Remote Sensing*, vol. 15, no. 11, p. 2787, 2023.

[5] N. Yokoya, N. Miyamura, and A. Iwasaki, "Preprocessing of hyperspectral imagery with consideration of smile and keystone properties," in *Multispectral, Hyperspectral, and Ultraspectral Remote Sensing Technology, Techniques, and Applications III*, A. M. Larar, H.-S. Chung, and M. Suzuki, Eds., vol. 7857, International Society for Optics and Photonics. SPIE, 2010, p. 78570B. [Online]. Available: https://doi.org/10.1117/12.870437

[6] X. Wang, X. Chen, Z. Zhao, Q. Pan, C. Luo, W. Shen, and M. Tang, "Effect of distortions on spectral signal acquisition of the grating imaging spectrometer," in *Sixth International Conference on Optical and Photonic Engineering (icOPEN 2018)*, Y. Yu, C. Zuo, and K. Qian, Eds., vol. 10827, International Society for Optics and Photonics. SPIE, 2018, p. 108272Z. [Online]. Available: https://doi.org/10.1117/12.2501128

[7] W. Bakker, H. v. d. Werff, and F. v. d. Meer, "Determining smile and keystone of lab hyperspectral line cameras," in *2019 10th Workshop on Hyperspectral Imaging and Signal Processing: Evolution in Remote Sensing (WHISPERS)*, 2019, pp. 1–5.

[8] D. Hu, C. Chen, H. Yang, A. Wang, G. Yue, Z. Gan, X. Chen, Y. Yan, Y. Zhong, Z. Xu, Z. Qu, P. Wang, T. Geng, S. Chen, and W. Sun, "Correction method for keystone distortion and smile distortion based on subpixel transformation," in *2024 IEEE Academic International Symposium on Optoelectronics and Microelectronics Technology (AISOMT)*, 2024, pp. 220–225.

[9] C. Heo, "Construction of a Hyperspectral Camera using Off-the-Shelf Parts and 3D-Printed Parts," Master's thesis, University of Arkansas, Fayetteville, 2019.

[10] M. B. Henriksen *et al.*, "Real-time corrections for a low-cost hyperspectral instrument," in *WHISPERS*, 2019.

[11] A. F. Hussein and A. AlBeladi, "Design and calibration of a low-cost benchtop pushbroom hyperspectral imaging system with conveyor-based scanning," *Results in Engineering*, p. 112126, 2026.

[12] M. Sameh, A. Hussein, and A. AlBeladi, "Hsi control suite: An integrated gui for operating and acquiring data from diy push-broom hyperspectral imaging systems," *SoftwareX*, vol. 34, p. 102680, 2026.

[13] M. B. Henriksen, E. F. Prentice, C. M. van Hazendonk, F. Sigernes, and T. A. Johansen, "Do-it-yourself VIS/NIR pushbroom hyperspectral imager with C-mount optics," *Optics Continuum*, vol. 1, no. 2, pp. 427–441, 2022.

[14] A. F. Hussein and A. AlBeladi, "Integrated calibration and distortion correction for a vis–nir pushbroom hyperspectral imaging system," *Available at SSRN 7533196*.